Topologically protected spatial-phase mismatching for cavity-enhanced quantum memories

Xia-Xia Li, Jia-Xin Wang, Yu-Hui Chen [*] and Xiangdong Zhang

Key Laboratory of advanced optoelectronic quantum architecture and measurements of Ministry of Education, Beijing Key Laboratory of Nanophotonics & Ultrafine Optoelectronic Systems, School of Physics, Beijing Institute of Technology, Beijing 100081, China

(Received 17 November 2023; revised 27 February 2024; accepted 20 March 2024; published 10 April 2024)

Microphotonic quantum memory presents a promising avenue for miniaturizing and scaling up memories for quantum network applications. While conventional microphotonic cavities can provide enhanced light-matter-interaction to improve the memory efficiency, they are constrained by inherent limitations when utilizing the quantum memory protocol of the revival of silenced echo (ROSE). These limitations primarily arise from the high sensitivity to cavity fabrication imperfections, which scatter stored optical modes into alternate modes and cause a subsequent reduction in efficiency. In this study, we propose that the incorporation of robust edge states and defect states in topological photonic crystals offers a solution to overcome this inherent limitation. The spatial-phase-mismatching effect that underlies ROSE is topologically protected, effectively mitigating the distortion of stored optical states caused by imperfection scattering and improves the memory efficiency.

DOI: 10.1103/PhysRevA.109.043511

I. INTRODUCTION

Quantum memory is an essential building block for synchronizing the information operations in quantum computation and extending the range of quantum communication. To date, quantum memories have been implemented in several different material platforms [1–5]. Among the promising candidates, memories based on solid-state materials doped with rare-earth ions, which offer the advantages of long coherence time [6–8], large inhomogeneous broadening [9]. and multiplexed memory capacities [10], are easy to integrate and extend due to its solid-state platform. Integrated quantum memory can overcome scalability and functionality limitations of macroscopic systems, facilitating large-scale quantum information processing. Crucially, the interconnection of integrated quantum memories with compact photonic components is vital for constructing scalable optical quantum networks.

Among the various memory schemes, the revival of the silenced echo (ROSE) protocol stands out for a combination of high performance and ease of operation [11]. Unlike other schemes, for example, the controlled reversible inhomogeneous broadening method [15,16] that requires large electric or magnetic gradient operations at the microscale, ROSE is an all-optical technique. This makes it compatible with various photonic integrated circuit components, such as waveguides, light sources, and detectors, facilitating the integration of ROSE-based quantum memories into existing photonic platforms.

However, the direct implementation of ROSE in microscale-integrated waveguide structures encounters reduced light absorption due to the shortened length of the optical path. This poses a considerable challenge in achieving high storage efficiency [12–16], particularly when employing a low ion doping concentration to ensure a long coherence time [17]. Efforts are being made to overcome this limitation by introducing microoptical cavities [18,19] to enhance the light-matter interactions. However, conventional photonic cavities have inherent limitations in the successful implementation of the ROSE memory. On one hand, the ROSE method relies on the spatial-phase-mismatching effect, which cannot be properly implemented in standing-wave cavities. On the other hand, even in the case of traveling-mode cavities like the whispering gallery mode (WGM) cavities, the presence of structural imperfections compromises the efficiency of the ROSE protocol. While a high-Q factor cavity is desired for maximizing light-matter interactions, it also implies high sensitivity to fabrication imperfections [20–23], resulting in cross-talk between the counterpropagating modes and ultimately reducing the overall efficiency of the ROSE protocol. The idea of using topologically protected non-Abelian zero modes to achieve robust quantum storage in ferromagnetic media has been proposed, but the formation of such modes requires several conditions to be met and special requirements are placed on the material [24].

Here, through an analysis of the requirements for the successful execution of ROSE, we propose that the robust edge states and defect states in topological photonic cavities can be used to address the limitations of conventional photonic cavities. In particular, we discuss the limitations of conventional standing-wave cavities and WGM cavities. In addition, based on erbium-doped lithium niobate thin film ($LiNbO_3$) material, we propose a photonic crystal design with topological boundary states for ROSE memory applications [25,26]. The spatial-phase-mismatching effect that ROSE relies on is topologically protected, effectively preventing distortion of the stored optical states caused by imperfection scattering. By leveraging the advantages of topological photonic cavities, we envision a significant improvement in the efficiency and robustness of the ROSE protocol for optical memories.

[*]stephen.chen@bit.edu.cn

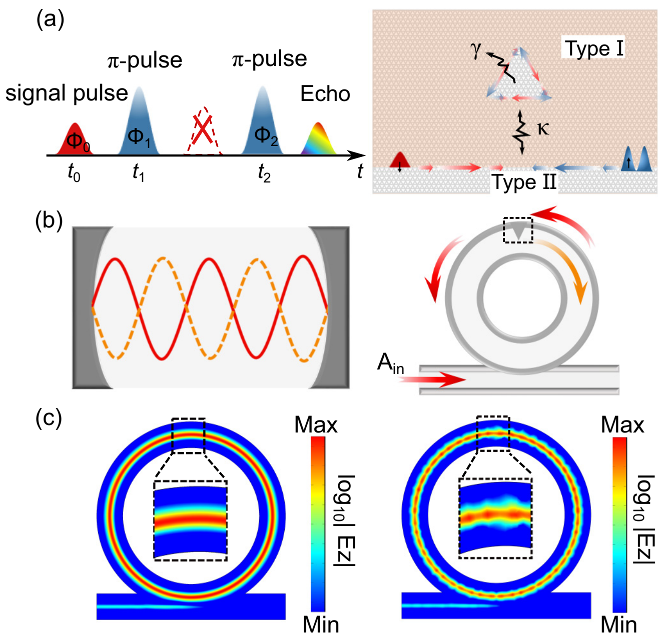

FIG. 1. Integrated topological quantum memory scheme. (a) Left, memory pulse sequence: red, a signal pulse with spatial phase ϕ_0; blue, two control π pulses with spatial phase: ϕ_1 and ϕ_2, respectively; rainbow, the photon echo. Right, a topologically protected cavity-waveguide memory, where κ and γ are the coupling coefficient of the cavity and the cavity intrinsic loss, respectively. (b) Left, schematics of a standing-wave cavity, which cannot provide the phase-mismatching effect for ROSE. Right, schematics of a conventional WGM cavity. A defect in the cavity causes the scattering of a clockwise propagating mode into a counterpropagating mode. (c) Comparison of electric field distribution (in log scale) without (left) and with (right) a defect in a WGM cavity.

II. THEORETICAL MODEL

The topological memory scheme is diagrammatically shown in Fig. 1(a). The pulse sequence used in our memory closely resembles that of the ROSE method. This sequence comprises an input signal pulse (depicted as red), succeeded by two control π pulses (depicted as blue). Due to the spatial-phase mismatch between the signal pulse and the control π pulses, the appearance of the first echo, which would otherwise occur in a conventional two-pulse echo scheme [11], is effectively canceled out. We employ this memory scheme in a topological photonic crystal structure that is based on an erbium-doped lithium niobate ($LiNbO_3$) thin film. The whole system consists of a microcavity interacting with a collection of N erbium ions, which are considered as two-level systems. The dynamical equation for the polarization of the erbium ions under the rotating frame is

$$\frac{d}{dt}\rho_{21}(\mathbf{r}) = (-i\Delta - \gamma_h)\rho_{21}(\mathbf{r}) + igae^{i\phi(\mathbf{r})}(\rho_{11} - \rho_{22}), \quad (1)$$

where a represents the field operator of the cavity mode, $\phi(\mathbf{r})$ is spatial phase distribution of the cavity mode, Δ is the frequency detuning of erbium ions, $\gamma_h = 1/T_2$ denotes the atomic homogeneous broadening and T_2 is the coherence time, g is the coupling strength of single erbium ion to single cavity photon, and $\rho_{11} - \rho_{22}$ indicates the population difference between the optical ground and excited state.

At the moment t_0, a signal pulse $A_{\rm in}(\mathbf{r}, t)$ with spatial phase distribution $\phi_0(\mathbf{r})$ is sent into the microcavity, which is mapped into the atomic ensemble in an absorbed manner. The coherent polarization of the atomic ensemble at the moment t_0^+ is

$$\rho_{21}(\mathbf{r}, t_0^+) = \frac{ig}{\sqrt{\kappa}}e^{i\phi_0(\mathbf{r})}\int_{-\infty}^{t_0} A_{in}(\mathbf{r}, t')e^{(i\Delta-\gamma_h)(t_0-t')}dt' \stackrel{\rm def}{=} Ce^{i\phi_0(\mathbf{r})}, \quad (2)$$

where C is a coefficient.

For $t_0 < t < t_1$, the atomic polarization undergoes free evolution

$$\rho_{21}(\mathbf{r}, t) = e^{-(i\Delta+\gamma_h)(t-t_0)}\rho_{21}(t_0^+). \quad (3)$$

.

Due to the inhomogeneous distribution of Δ, each atom accumulates different phase over time the coherence of the atomic ensemble will gradually decrease. At t_1, a control π pulse is used to resemble the dephased (in time) atomic coherence. The first π pulse has a spatial phase $\phi_1(\mathbf{r})$ that is different from $\phi_0(\mathbf{r})$. Such a π pulse not only reverses the phase of the collective atomic polarization, but also introduces an additional phase factor $2i\phi_1(\mathbf{r})$ associated with the π pulse itself such that

$$\rho_{21}(t_1^+) = e^{2i\phi(\mathbf{r})}\rho_{21}^*(t_1^-). \quad (4)$$

For $t_1 < t < t_2$, the atomic polarization again undergoes free evolution. We have

$$\rho_{21}(\mathbf{r}, t) = C^*e^{-i\phi_0(\mathbf{r})+2i\phi_1(\mathbf{r})}e^{i\Delta(t-2t_1+t_0)}e^{-\gamma_h(t-t_0)}. \quad (5)$$

If the spatial phase of the signal pulse and control π pulse are identical, i.e., $\phi_0(\mathbf{r}) = \phi_1(\mathbf{r})$, the atomic phase promptly returns to its initial state at $t = 2t_1 - t_0$. As a result, the system polarization reaches its maximum and emits an echo, known as a two-pulse photon echo. However, the two-pulse photon echo is not suitable for optical quantum storage because the first π pulse also causes atomic population inversion, which, in combination with spontaneous radiation noise, ultimately reduces the fidelity of the quantum storage [27,28]. The ROSE memory protocol relies on the spatial phase mismatch $\phi_0(\mathbf{r}) \neq \phi_1(\mathbf{r})$ to build a destructive interference of the emissions from different atoms and silence the amplified echo, as illustrated in the red dashed line in Fig. 1(a).

At t_2, a second π pulse with phase $\phi_2(\mathbf{r})$ is sent into the cavity. The atomic coherence becomes

$$\rho_{21}(\mathbf{r}, t^+) = Ce^{i\phi_0(\mathbf{r})-2i\phi_1(\mathbf{r})+2i\phi_2(\mathbf{r})}e^{i\Delta(t-2t_2+2t_1-t_0)}e^{-\gamma_h(t-t_0)}. \quad (6)$$

If $\phi_1(\mathbf{r}) = \phi_2(\mathbf{r})$ for the two π pulses are the same, the ensemble polarization can be recalled at $t_{\rm e} = 2t_2 - 2t_1 + t_0$:

$$\rho_{21}(\mathbf{r}, t_{\rm e}) = Ce^{i\phi_0}e^{-\gamma_h(t_{\rm e}-t_0)}. \quad (7)$$

After the application of a second π pulse, the population inversion caused by the first pulse is inverted back to the original ground-state population. As a result, the second echo, which is emitted from the ground state, reliably retains the information that was encoded in the signal pulse [29].

In the implementation of ROSE in bulk materials, the signal pulse and control pulses are input from two different directions [30]. However, this method faces difficulties when implemented in microphotonic cavities. One major challenge is that it becomes challenging to satisfy the requirements on phase distribution $\phi_0(\mathbf{r}) \neq \phi_1(\mathbf{r}) = \phi_2(\mathbf{r})$ in conventional photonic cavities. On one hand, such a requirement cannot be met in standing-wave cavities. Because the mode profile of the standing cavity mode has a constant phase distribution, which implies that $\phi_0 = \phi_1 = \phi_2 = \text{const.}$, as shown on the left side of Fig. 1(b). Consequently, the first echo in Eq. (5) cannot be canceled.

On the other hand, although it is possible to realize ROSE in a conventional WGM cavity, as depicted in the right panel of Fig. 1(b), achieving high readout efficiency critically relies on the high perfection of the microcavity structure. WGM cavities support degenerate clockwise (CW) and counterclockwise (CCW) modes, allowing for the fulfillment of the requirement $\phi_0(\mathbf{r}) \neq \phi_1(\mathbf{r}) = \phi_2(\mathbf{r})$ by utilizing the CW and CCW modes. However, even small defects or imperfections in the cavity, which are inevitable during the fabrication process, can cause cross-talk between the CW and CCW modes [20]. This means that a defect in the cavity scatters the stored signal optical state, for example, a CW mode, into a CCW mode. Figure 1(c) illustrates how the distribution of a high-Q-factor WGM mode is affected by a defect in the cavity. It is evident that a perfect WGM mode exhibits a well-defined traveling characteristic, while a 100-nm defect leads to cross-talk between the CW and CCW modes, resulting in a standing-wave feature. This cross-talk impedes the fulfillment of the spatial phase requirements for ROSE storage, making it unfavorable for high-efficiency quantum storage implementation.

III. RESULTS AND DISCUSSION

To address the challenges associated with conventional photonic cavities, we utilize topological photonic cavities that possess robust edge states and defect states to realize high-efficiency optical quantum memory, as shown in the right panel of Fig. 1(a). In this setup, a topological microcavity supporting degenerate CW and CCW modes is coupled to a topological waveguide. This configuration takes advantage of the topological properties of the cavity and waveguide to achieve efficient and reliable storage and retrieval of quantum information.

The study of our topological optical quantum memory is based on a two-dimensional valley-Hall topological photonic crystal, which is composed of a honeycomb lattice of triangular holes. The rhombic cell has two types of triangular holes with different side lengths, as depicted in the inset of Fig. 2(a), where $d_1 = 0.8a$ and $d_2 = 0.35a$. The lattice constant $a = 575$ nm. The refractive index of the $LiNbO_3$ thin film substrate is set to $n = 2.21$ [31]. By rotating the unit cell by 180 degrees and periodically arranging each type of unit cell, two types of photonic crystals are formed, denoted as type I and type II on the right side of Fig. 2(a), respectively. These two types of photonic crystals exhibit opposite signs of the topological index.

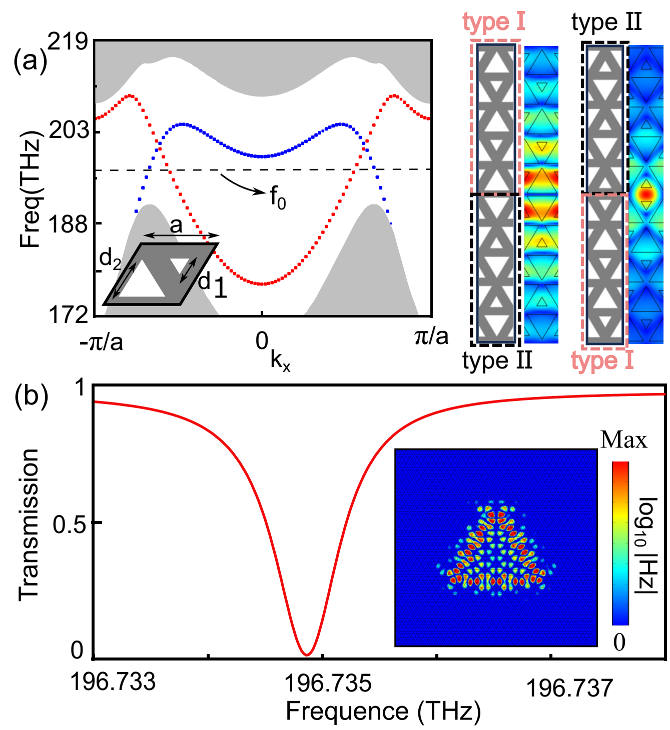

FIG. 2. Valley-dependent edge states in topological photonic crystal cavity. (a) Left, dispersion of the valley-dependent edge states for two distinct domain walls as shown on the right. Here, the black dashed line corresponds to a traveling-wave mode with eigenfrequency $f_0 = 196.73486$ THz (1.5 μm) of the topological cavity in (b). Right, the structure of supercells comprised of two types of photonic crystal named type I and type II. Their field distributions (in log scale) around the two different interfaces. The first one corresponds to the red dispersion curve on the left and the second one corresponds to the blue. (b) Transmission spectra for the triangular cavity. Inset: The field distribution (in log scale) of the topological cavity mode at the resonant frequency f_0. The side length of the cavity is $12a$.

When the boundaries of the two types of photonic crystals are connected together, localized nontrivial edge states emerge at the interface, as observed in previous works [32–34]. Figure 2(a) illustrates two types of waveguide modes at the valley interfaces, represented by the red and blue dispersion curves. On the right-hand side of Fig. 2(a), the field distributions of these two transverse-electric modes are shown. The linear dispersion relation indicates that this topological photonic crystal supports valley-locked interface states. These states are robust against small structural defects within the crystal because the coupling between different valley states that is well-separated in momentum space are extremely weak [35,36].

Based on these properties of the valley edge states, we design a triangular cavity with a side length of $12a$. The cavity is composed of a type-II photonic crystal surrounded by a type-I photonic crystal, where the definitions of type I and type II are the same as those in Fig. 2(a). The field distribution of such a cavity, as shown in the inset of Fig. 2(b), is primarily confined to the interface between the two types of photonic crystals. The cavity has a resonance wavelength of 1.5 μm and demonstrates an intrinsic quality factor $Q_{\rm int}$ of 1×10^9, along with a loaded quality factor Q_{load} of 2.7×10^5 (in this case, the doping concentration of erbium ions in $LiNbO_3$ is set at 97 ppm). Additionally, due to the spatial rotation symmetry, this cavity mode exhibits a two-fold degeneracy, resulting in a Poynting vector that flows either CW or CCW along the cavity boundary [37,38].

As aforementioned, these two degenerate modes are generally decoupled from each other, highlighting the robustness of the topological structure. Leveraging these effects, we develop our ROSE memory scheme based on topological photonic crystals, following similar pulse sequences as shown in Fig. 1(a).

At time t_0, a weak signal pulse propagates to the right, as depicted in Fig. 1(a). This pulse is excited by placing an electric point dipole with right-circular polarization near the waveguide boundary at a high symmetry point, enabling directional coupling to the edge state. The spin direction of the dipole is denoted by the black arrow. Subsequently, the signal light field is coupled into the cavity and travels along it in a CW direction. Note that the coupling between the cavity and the waveguide is tunable. This adjustable coupling plays a crucial role in determining the absorption quality of the input pulse, which, in turn, impacts the storage efficiency of the memory. Furthermore, it also affects the ability to effectively cancel the first echo in ROSE through destructive interference. To manipulate the coupling, several controllable parameters can be adjusted. These include modifying the waveguide-cavity distance, changing the periodicity, and/or the size of the holes between the waveguide and the cavity. Implementing these adjustments enables the fine-tuning of the coupling. Subsequently, a critical coupling between the waveguide and the cavity is achieved according to the absorption of light by the 97-ppm erbium ions in $LiNbO_3$.

At time t_1 and t_2, π pulses counterpropagating with the incoming signal with left-circular polarization enters the cavity. The two field distributions in Figs. 3(a) and 3(b) are a pair of degenerate cavity modes in an orthogonal manner, exhibiting a phase mismatch in space. As mentioned earlier, an echo that would normally be emitted after the first π pulse is suppressed within the cavity due to atomic coherent collapses caused by the spatial phase mismatch. In this scenario, an echo of the signal pulse is emitted from the cavity and propagates to the right at t_3.

Ensuring the effective operation of ROSE in integrated quantum memory systems relies on two key factors. First, it requires a spatial phase mismatch between the input and control pulses, as shown on the lower level of Figs. 3(c) and 3(d). This phase difference is essential for suppressing the emission of an echo signal during the control pulse, and allowing its subsequent release during the retrieval stage. Second, it also relies on the spatial intensity overlap between the input and control pulses, ensuring that both fields interact with the same atoms. We plot the field distributions (in log scale) for the two counterpropagating modes on the upper level of Figs. 3(c) and 3(d), which illustrate nearly identical field distributions of the two modes, ensuring that the desired coherent processes can occur.

Achieving the necessary balance between spatial intensity matching and spatial phase mismatch in microphotonic

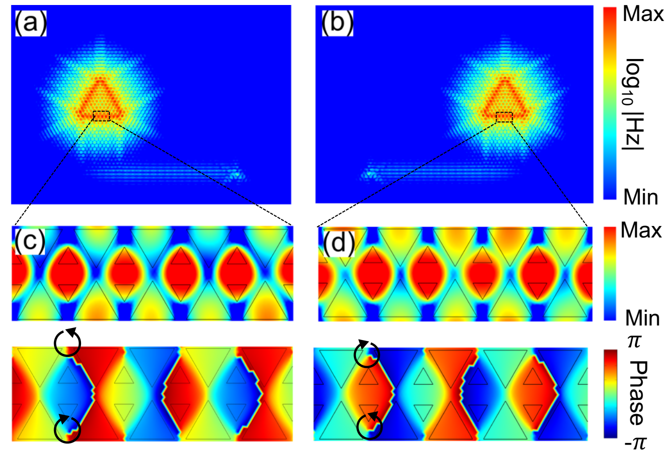

FIG. 3. Mode analysis of topological waveguide-cavity system. (a), (b) Cavity field distributions (in log scale) that excited by left and right circularly polarized chiral source placed on the left and right sides of the waveguide, respectively. (c), (d) Up, the zoomed field distributions corresponding to the black dashed boxes in (a), (b). The high-field-intensity points appear in same locations. Down, the phase distribution corresponding to the black dashed boxes in (a), (b). The phase vortex (black arrows) at the relative positions of the valley photonic crystal interface is opposite.

cavities poses a significant challenge. This difficulty is amplified when a high-Q cavity is required to improve memory efficiency, as a higher-Q value increases sensitivity to fabrication imperfections. To provide a more detailed illustration of this delicate balance, we present the intensity overlap and phase overlap for the CW and CCW modes of the two imperfect cavities in Table I. Both cavities were fabricated using the same material to ensure nearly identical Q factors.

In the case of conventional WGM cavities, as shown in Fig. 1(a), with a Q factor of 2×10^5, a mere 7% imperfection (resulting from a core width of 0.245 μm and a defect diameter of 0.017 μm) can reduce the phase overlap to 32% (calculated using the formula $\int_V e^{i\phi_1(r)-i\phi_0(r)} dr/V$, where V is the cavity's mode volume) and the intensity overlap to 96%. Additionally, we evaluate the output intensity of the ROSE storage protocol on this imperfect WGM cavity, as shown at the top of Fig. 4(a). It is evident that, when the condition of spatial phase mismatch is not met, the first unwanted echo emerges, subsequently diminishing the efficiency of the second echo. These challenges present obstacles to the practical implementation

TABLE I. Overlaps in field intensity and spatial phase for the CW and CCW modes in different cavities with defects.

	Conventional	Topological[a]
Intensity	96%	99%
Phase	32%	5%

[a]Calculations for a cavity containing three defects as depicted in Fig. 4(b). If the number of defects increases to five, the overlap in intensity and phase becomes 98.2% and 5.7%, respectively.

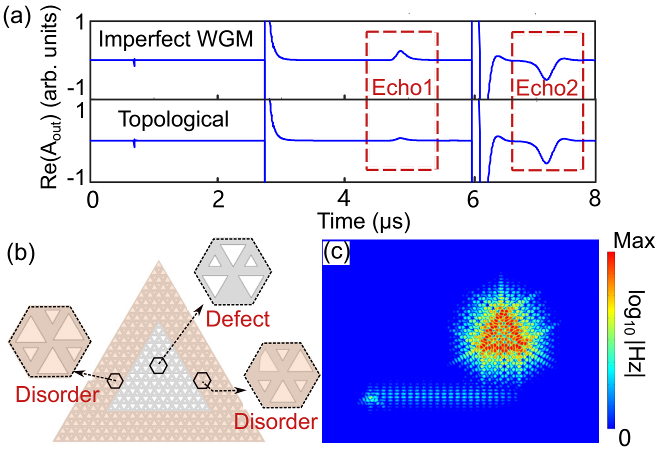

FIG. 4. Topological photonic crystal quantum memory. (a) Output pulse sequences of photon echo schemes based on the imperfect WGM cavity in Fig. 1(c) (upper) and topological photonic crystal cavity (lower). The red dashed lines indicate the positions of the first (unwanted) and second echoes. (b) The schematic diagram of the cavity-waveguide coupling system with missing, shift, incompletion defects in different locations as noted. (c) The robust field distributions (in log scale) with the aforementioned defects.

of ROSE in traditional integrated quantum memory systems, thereby limiting memory efficiency to 68%.

However, in the case of the topological photonic cavity with similar Q factor depicted in Fig. 3, its resistance to backscattering from defects provide solutions to overcoming the aforementioned challenges. We examine the robustness of the system when exposed to various defects within the cavity. Figure 4(b) provides a visualization of the defects introduced, including the removal of a cell within the cavity, the shift of another cell at the cavity boundary, and a change on the shape of another cell. Remarkably, Fig. 4(c) demonstrates that these defects have a weak impact on the field distribution inside the cavity. This observation suggests that even in the presence of missing or disordered defects at different positions within the cavity, the field distribution remains largely unaffected. To quantify the effects of these defects, we compute the overlaps for the CW and CCW modes, as outlined in Table I. Additionally, we assess the output intensity of the ROSE storage protocol on this perturbed topological cavity, depicted at the bottom of Fig. 4(a). These results clearly indicate that small defects have minimal influence on the amplitude and phase distribution of the optical field, ensuring the perfectly silenced amplified echo. Moreover, even with the number of defects increased to five unit cells around the triangular cavity, its robustness remains, as shown in Table I, highlighting the topological cavity's ability to withstand defects of varying sizes.

IV. CONCLUSION

In conclusion, we propose an on-chip topologically protected optical quantum memory scheme based on erbium-doped lithium niobate topological photonic crystals. This scheme utilizes two selectively excited degenerate resonant modes in a topological photonic cavity to distinguishably represent signal pulses and π pulses. The topological edge state in the cavity prohibits the cross-talk between the two degenerate cavity modes and provides immunity to defect scattering, offering high-efficiency storage and retrieval of the ROSE protocol. Additionally, the compact size of the topological photonic crystals enables easy integration with existing devices, making them suitable for large-scale applications in quantum networks.

ACKNOWLEDGMENTS

The authors wish to acknowledge financial support from the National Natural Science Foundation of China (Grants No. 12174026 and No. 62105033), the Start-up Fund of Beijing Institute of Technology, and the Science and Technology Innovation Project of Beijing Institute of Technology.

[1] H. P. Specht, C. Nölleke, A. Reiserer, M. Uphoff, E. Figueroa, S. Ritter, and G. Rempe, A single-atom quantum memory, Nature (London) **473**, 190 (2011).

[2] D. L. Moehring, P. Maunz, S. Olmschenk, K. C. Younge, D. N. Matsukevich, L.-M. Duan, and C. Monroe, Entanglement of single-atom quantum bits at a distance, Nature (London) **449**, 68 (2007).

[3] Y. Yu, F. Ma, X.-Y. Luo, B. Jing, P.-F. Sun, R.-Z. Fang, C.-W. Yang, H. Liu, M.-Y. Zheng, and X.-P. Xie, Entanglement of two quantum memories via fibres over dozens of kilometres, Nature (London) **578**, 240 (2020).

[4] M. Hosseini, B. M. Sparkes, G. Campbell, P. K. Lam, and B. C. Buchler, High efficiency coherent optical memory with warm rubidium vapour, Nat. Commun. **2**, 174 (2011).

[5] X.-X. Li, P. Zhou, Y.-H. Chen, and X.-D. Zhang, Integrated optical quantum memory controlled by the electro-optic effect, Phys. Rev. A **108**, 012614 (2023).

[6] Y.-H. Chen, X. Fernandez-Gonzalvo, and J. J. Longdell, Coupling erbium spins to a three-dimensional superconducting cavity at zero magnetic field, Phys. Rev. B **94**, 075117 (2016).

[7] Y.-Z. Ma, M. Jin, D.-L. Chen, Z.-Q. Zhou, C.-F. Li, and G.-C. Guo, Elimination of noise in optically rephased photon echoes, Nat. Commun. **12**, 4378 (2021).

[8] Y.-H. Chen, X. Fernandez-Gonzalvo, S. P. Horvath, J. V. Rakonjac, and J. J. Longdell, Hyperfine interactions of Er^{3+} ions in Y_2SiO_5: Electron paramagnetic resonance in a tunable microwave cavity, Phys. Rev. B **97**, 024419 (2018).

[9] X. Liu, J. Hu, Z.-F. Li, X. Li, P.-Y. Li, P.-J. Liang, Z.-Q. Zhou, C.-F. Li, and G.-C. Guo, Heralded entanglement distribution between two absorptive quantum memories, Nature (London) **594**, 41 (2021).

[10] C. Laplane, P. Jobez, J. Etesse, N. Gisin, and M. Afzelius, Multimode and long-lived quantum correlations between photons and spins in a crystal, Phys. Rev. Lett. **118**, 210501 (2017).

[11] V. Damon, M. Bonarota, A. Louchet-Chauvet, T. Chanelière, and J.-L. Le Gouët, Revival of silenced echo and quantum memory for light, New J. Phys. **13**, 093031 (2011).

[12] T. Zhong, J. M. Kindem, J. G. Bartholomew, J Rochman, I. Craiciu, E. Miyazono, M. Bettinelli, E. Cavalli, V. Verma, S. W. Nam, F. Marsili, M. D. Shaw, A. D. Beyer, and A. Faraon, Nanophotonic rare-earth quantum memory with optically controlled retrieval, Science **357**, 1392 (2017).

[13] J. V. Rakonjac, G. Corrielli, D. Lago-Rivera, A. Seri, M. Mazzera, S Grandi, R. Osellame, H. D. Riedmatten, Storage and analysis of light-matter entanglement in a fiber-integrated system, Sci. Adv. **8**, eabn3919 (2022).

[14] I. Craiciu, M. Lei, J. Rochman, J. G. Bartholomew, and A. Faraon, Multifunctional on-chip storage at telecommunication wavelength for quantum networks, Optica **8**, 114 (2021).

[15] C. Liu, Z.-Q. Zhou, T.-X. Zhu, L. Zheng, M. Jin, X. Liu, P.-Y. Li, J.-Y. Huang, Y. Ma, T. Tu, T.-S. Yang, C.-F. Li, and G.-C. Guo, Reliable coherent optical memory based on a laser-written waveguide, Optica **7**, 192 (2020).

[16] D.-C. Liu, P.-Y. Li, T.-X. Zhu, L. Zheng, J.-Y. Huang, Z.-Q. Zhou, C.-F. Li, and G.-C. Guo, On-demand storage of photonic qubits at telecom wavelengths, Phys. Rev. Lett. **129**, 210501 (2022).

[17] Y.-H. Chen, S. P. Horvath, J. J. Longdell, and X.-D. Zhang, Optically unstable phase from ion-ion interactions in an erbium-doped crystal, Phys. Rev. Lett. **126**, 110601 (2021).

[18] M. M. Minnegaliev, K. I. Gerasimov, R. V. Urmancheev, A. M. Zheltikov, and S. A. Moiseev, Linear Stark effect in $Y_3Al_5O_{12}$: Tm^{3+}crystal and its application in the addressable quantum memory protocol, Phys. Rev. B **103**, 174110 (2021).

[19] E. S. Moiseev, A. Tashchilina, S. A. Moiseev, and B. C. Sanders, Broadband quantum memory in a cavity via zero spectral dispersion, New J. Phys. **23**, 063071 (2021).

[20] J. Zhu, C. Wang, C. Tao, Z. Fu, H. Liu, F. Bo, L. Yang, G. Zhang, and J. Xu, Imperfect chirality at exceptional points in optical whispering-gallerymicrocavities, arXiv:2208.07077.

[21] S. Ya. Prislopski, E. K. Naumenko, I. M. Tiginyanu, L. Ghimpu, E. Monaico, L. Sirbu, and S. V. Gaponenko, Anomalous retroreflection from strongly absorbing nanoporous semiconductors, Opt. Lett. **36**, 3227 (2011).

[22] A. Mazzei, S. Götzinger, L. de S. Menezes, G. Zumofen, O. Benson, and V. Sandoghdar, Controlled coupling of counter-propagating whispering-gallery modes by a single Rayleigh scatterer: A classical problem in a quantum optical light, Phys. Rev. Lett. **99**, 173603 (2007).

[23] T. Zhang, J. Sun, Y. X. Yang, and Z. X. Li, Photonic crystal filter based on defect mode and waveguide mode symmetry matching, Opt. Commun. **428**, 53 (2018).

[24] K. Agarwal, Quantum Hall valley ferromagnets as a platform for topologically protected quantum memory, Phys. Rev. B **107**, 125163 (2023).

[25] Q. Cheng, S. T. Wang, J. T. Lv, and N. Liu, Topological photonic crystal biosensor with valley edge modes based on a silicon-on-insulator slab, Opt. Express **30**, 10792 (2022).

[26] C.-C. Lu, Y.-Z. Sun, C.-Y. Wang, H.-Y. Zhang, W. Zhao, X.-Y. Hu, M. Xiao, W. Ding, Y.-C. Liu, and C. T. Chan, On-chip nanophotonic topological rainbow, Nat. Commun. **13**, 2586 (2022).

[27] Y. Ma, Y.-Z. Ma, Z.-Q. Zhou, C.-F. Li, and G.-C. Guo, One-hour coherent optical storage in an atomic frequency comb memory, Nat. Commun. **12**, 2381 (2021).

[28] S. A. Moiseev and B. S. Ham, Photon-echo quantum memory with efficient multipulse readings, Phys. Rev. A **70**, 063809 (2004).

[29] Y. Fu, M.-F. Wang, and Y.-Z. Zheng, Cavity-assisted revival of silenced echo quantum memory, Opt. Commun. **321**, 162 (2014).

[30] J. Dajczgewand, J. L. Le Gouët, A. Louchet-Chauvet, and T. Chanelière, Large efficiency at telecom wavelength for optical quantum memories, Opt. Lett. **39**, 2711 (2014).

[31] S. Wang, L. Yang, M. Shen, W. Fu, Y. Xu, R. L. Cone, C. W. Thiel, and H. X. Tang, Er : $LiNbO_3$ with high optical coherence enabling optical thickness control, Phys. Rev. Appl. **18**, 014069 (2022).

[32] Y.-H. Yang, Y.-C. Yamagami, X.-B. Yu, P. Pitchappa, J. Webber, B. Zhang, M. Fujita, T. Nagatsuma, and R. Singh, Terahertz topological photonics for on-chip communication, Nat. Photon. **14**, 446 (2020).

[33] A. B. Khanikaev and G. Shvets, Two-dimensional topological photonics, Nat. Photon. **11**, 763 (2017).

[34] H.-R. Xue, Y.-H. Yang, and B.-L. Zhang, Topological valley photonics: Physics and device applications, Adv. Photon. Res. **2**, 2100013 (2021).

[35] X.-T. He, E.-T. Liang, J.-J. Yuan, H.-Y. Qiu, X.-D. Chen, F.-L. Zhao, and J.-W. Dong, A silicon-on-insulator slab for topological valley transport, Nat. Commun. **10**, 872 (2019).

[36] J. W. You, Z. H. Lan, Q. Ma, Z. Gao, Y. H. Yang, F. Gao, M. Xiao, and T. J. Cui, Topological metasurface: from passive toward active and beyond, Photon. Res. **11**, B65 (2023).

[37] L. He, W. X. Zhang, and X. D. Zhang, Topological all-optical logic gates based on two-dimensional photonic crystals, Opt. Express **27**, 25841 (2019).

[38] Y.-Q. Zeng, U. Chattopadhyay, B.-F. Zhu, B. Qiang, J.-H. Li, Y.-H. Jin, L.-H. Li, A. G. Davies, E. H. Linfield, Baile Zhang, Y.-D. Chong, and Q.-J. Wang, Electrically pumped topological laser with valley edge modes, Nature (London) **578**, 246 (2020).